Bond order via cavity-mediated interactions

Titas Chanda,[1,2] Rebecca Kraus,[3] Jakub Zakrzewski,[2,4] and Giovanna Morigi[3]
[1]*The Abdus Salam International Centre for Theoretical Physics (ICTP), Strada Costiera 11, 34151 Trieste, Italy*
[2]*Institute of Theoretical Physics, Jagiellonian University in Krakow, Łojasiewicza 11, 30-348 Kraków, Poland*
[3]*Theoretical Physics, Department of Physics, Saarland University, 66123 Saarbrücken, Germany*
[4]*Mark Kac Complex Systems Research Center, Jagiellonian University in Kraków, Łojasiewicza 11, 30-348 Kraków, Poland*

(Received 18 January 2022; revised 8 August 2022; accepted 9 August 2022; published 22 August 2022)

We numerically study the phase diagram of bosons tightly trapped in the lowest band of an optical lattice and dispersively coupled to a single-mode cavity field. The dynamics is encompassed by an extended Bose-Hubbard model. Here, the cavity-mediated interactions are described by a two-body potential term with a global range and by a correlated tunneling term where the hopping amplitude depends on a global observable. We determine the ground-state properties in one dimension by means of the density matrix renormalization group algorithm, focusing on the effects due to the correlated tunneling. The latter is responsible for the onset of bond orders, manifesting in one insulating and two gapless bond-ordered phases. We discuss the resulting phases for different geometries that correspond to different relative strengths of the correlated tunneling coefficient. We finally analyze the scaling of the entanglement entropy in the gapless bond-ordered phases that appear entirely due to global interactions and determine the corresponding central charges.

DOI: 10.1103/PhysRevB.106.075137

I. INTRODUCTION

Ultracold atomic gases in optical lattices realize the strongly correlated dynamics of the Hubbard model with tunable interactions [1–5]. The dispersive coupling with a high-finesse resonator, additionally, allows one to design interactions whose range can be tailored and whose strength can be tuned [6,7]. One prominent example is the all-to-all interaction in a quantum gas of bosons realized by coupling an electric dipole transition with a single-mode resonator [8]. Here, the appearance of phases with density modulations was observed by tuning the effective strength of the coupling with the cavity. These patterns support coherent scattering into the cavity mode [8] and can be either superfluid or incompressible. The experimentally measured phases are captured by the ground state of an extended Bose-Hubbard model with global interactions, as shown in Refs. [9–12]. This model describes the effect of the cavity-mediated potential by means of an interaction term between a pair of sites that depends on the on-site density and has a global range.

Ab initio derivations of the Bose-Hubbard model show, however, that two-body interactions give rise to further terms describing correlated tunneling [13–18]. These contributions can be important in determining the phase of superconductors [19–21], frustrated quantum magnets [22,23], and dipolar gases [14,15,24–26]. They can interfere with single-particle hopping [18,26,27] and, in the cavity quantum electrodynamics (QED) setup, give rise to an effective periodic modulation of the bonds. Indeed, at half filling this interference is at the basis of the emergence of self-organized topological insulating phases [18].

In this work, we characterize the quantum ground state of the extended Bose-Hubbard model of cavity QED taking into account both the cavity-induced density-density and correlated hopping terms for different lattice geometries. We consider a one-dimensional lattice and determine the quantum phases for half and unit fillings using the density matrix renormalization group (DMRG) algorithm [28–31] extended to the case of global interactions [18,32]. We show that correlated tunneling gives rise to a bond order that can be supersolid, superfluid, or insulating. We analyze, in particular, the scaling of the entanglement entropy at the bond superfluid and bond supersolid phases. Our analysis complements and extends the study of Ref. [18] by investigating the phase diagram for generic geometries. These geometries were also considered in Ref. [17] where the ground state of atoms in small chains using exact diagonalization was discussed.

The paper is organized as follows. In Sec. II we review the extended Bose-Hubbard model of cavity QED and discuss the dependence of its coefficients on the cavity system parameters. In Sec. III, we present the ground-state phase diagrams calculated by means of the DMRG approach and analyze the nature of the phase transitions. We then perform the scaling analysis of the entanglement entropy in the gapless bond-ordered phases that are stabilized entirely by the cavity-mediated global terms. The conclusions are drawn in Sec. IV. The Appendixes provide details on the determination of the coefficients of the extended Bose-Hubbard model.

II. EXTENDED BOSE-HUBBARD MODEL WITH CAVITY-MEDIATED INTERACTIONS

The system we consider consists of N bosons tightly bound in the lowest band of a one-dimensional optical lattice with L sites. Let $\hat{a}_i$ and $\hat{a}_i^\dagger$ denote the bosonic operators destroying and creating, respectively, a boson at site $i = 1, \ldots, L$ with

$[\hat{a}_i, \hat{a}_j^\dagger] = \delta_{i,j}$, and $\hat{n}_i = \hat{a}_i^\dagger \hat{a}_i$ being the corresponding particle number operator. The Hamiltonian $\hat{H}_{\rm EBH}$ determining their dynamics is the one of the extended Bose-Hubbard model [17,33],

$$\hat{H}_{\rm EBH} = \hat{H}_{\rm BH} + \hat{H}^C_{\rm BH}, \tag{1}$$

which is the sum of the standard Bose-Hubbard Hamiltonian $\hat{H}_{\rm BH}$,

$$\hat{H}_{\rm BH} = -t \sum_j (\hat{a}_j^\dagger \hat{a}_{j+1} + {\rm H.c.}) + \frac{U}{2} \sum_j \hat{n}_j(\hat{n}_j - 1), \tag{2}$$

and of the terms containing the cavity-mediated interactions [13,17],

$$\hat{H}^C_{\rm BH} = \frac{U_1}{L}(z^2 \hat{D}^2 + zy(\hat{D}\hat{B} + \hat{B}\hat{D}) + y^2 \hat{B}^2). \tag{3}$$

The details of the derivation of Hamiltonian (3) follow from Refs. [10,33,34] and are reported in Ref. [18] (see also Appendix A). The coefficients in Eq. (2) are positive and are the nearest-neighbor hopping rate t and the strength of the on-site repulsion U. The coefficient U_1 scaling the cavity term in Eq. (3) can be either positive or negative; the factor $1/L$ warrants extensivity [13,33]. Operators $\hat{D}$ and $\hat{B}$ depend on the on-site densities and hoppings, respectively [17,18]:

$$\hat{D} = \sum_j (-1)^j \hat{n}_j, \tag{4}$$

$$\hat{B} = \sum_i (-1)^i (\hat{a}_{i+1}^\dagger \hat{a}_i + {\rm H.c.}), \tag{5}$$

where the staggered sum emerges when the cavity wavelength is twice the lattice periodicity [10,33]. The coefficients y and z are dimensionless parameters whose strength depends on the setup's geometry and are discussed in the following.

We note that the term $\hat{D}^2$ is a global density-density interaction, that promotes the onset of a population imbalance between even sites (with $j = 2n$) and odd sites (with $j = 2n + 1$) [8–10]. The two other terms, $\hat{D}\hat{B} + \hat{B}\hat{D}$ and $\hat{B}^2$, describe correlated tunneling processes induced by the cavity field.

A. Bose-Hubbard coefficients

The coefficients in Eq. (1) are numerically calculated from the overlap integrals using the Wannier functions of the lowest band of the static optical lattice. In our calculations they are varied taking into account that in the experiment the control parameters are the depth of the optical lattice, the s-wave scattering length, and the cavity interaction amplitude and its sign. When we sweep across the phase diagram, we keep fixed the lattice depth at the value $V_0 = 4E_R$, where $E_R = \hbar^2 k^2/(2m)$ is the recoil energy for atoms of mass m, and k the lattice and cavity wave number. Therefore, in our numerical calculations the tunneling coefficient is kept constant. The ratio t/U is varied by tuning U via the s-wave scattering length. The sign of the detuning between cavity and driving laser determines the sign of the coefficient U_1. Moreover, the detuning and the strength of the cavity field determine the magnitude of $|U_1|$ [13,33–35]. Thus, in our calculations the ratios U_1/U and t/U are varied by simultaneously changing U_1 and U.

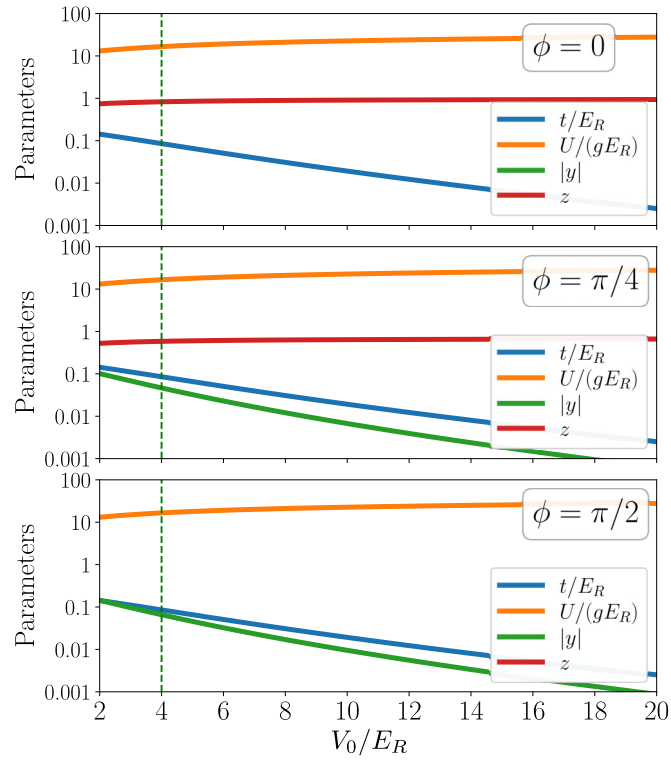

FIG. 1. The coefficients z, $|y|$, t/E_R, and $U/(gE_R)$ as a function of the lattice depth V_0, in units of the recoil energy E_R, for $\phi = 0$ (upper panel), $\phi = \pi/4$ (middle panel), and $\phi = \pi/2$ (lower panel). The vertical dashed line corresponds to the lattice depth of $V_0 = 4E_R$. The coefficient g scaling the on-site repulsion coefficient contains the physical variables including the scattering length; therefore, $U/(gE_R)$ is the overlap integral solely depending on the Wannier functions, which in turn are determined by V_0.

The coefficients y and z in Eq. (3) are overlap integrals between the Wannier functions $w_j(x)$ and the cavity mode function $\cos(kx + \phi)$ (see Appendix A):

$$z = \int_0^{aL} dx\, w_j(x)^2 \cos(kx + \phi),$$
$$y = \int_0^{aL} dx\, w_j(x) w_{j+1}(x) \cos(kx + \phi), \tag{6}$$

where j denotes the lattice site about which the Wannier function is centered, a is the lattice periodicity, $a = \pi/k$, and ϕ is the phase shift between the lattice and the cavity standing wave. The phase shifts $\phi = 0$ and $\phi = \pi/2$ correspond to trapping the atoms at the antinodes and at the nodes, respectively, of the cavity standing wave. This is realized by tuning the laser either on the blue or on the red side of the cavity resonance. In this paper we will also consider the case $\phi = \pi/4$, for which both y and z are different from zero. We remark that $y \leqslant 0$ for the parameter regimes we inspect.

Figure 1 displays the coefficients z and $|y|$ as a function of V_0 for the three different phase shifts $\phi = 0$, $\pi/4$, and $\pi/2$ considered in this paper. We also display the tunneling rate t and the on-site coefficient U for comparison, keeping in mind that these quantities are independent of ϕ. The upper panel shows the parameters for $\phi = 0$, where the y coefficient vanishes within machine precision. For $\phi = \pi/4$ both y and

z are finite: the z coefficient is almost independent of the lattice depth V_0, while $|y|$ decreases monotonically with V_0. For $\phi = \pi/2$ (see lower panel) the z coefficient is zero within machine precision. The vertical dashed line in Fig. 1 indicates the value of V_0 considered in this work. For $\phi = 0$ the values of the overlap integrals are given by $z = 0.8279$ and $y = 0$; thus we neglect the correlated tunneling. For $\phi = \pi/2$ we find $y = -0.0658$ and $z = 0$. In this case the cavity-mediated interactions are solely described by the term proportional to $\hat{B}^2$. Setting $\phi = \pi/4$ the overlap integrals are $z = 0.5854$ and $y = -0.0465$ and we expect to observe an interplay between the density-density potential and the correlated tunneling.

B. Observables

The ground state of Hamiltonian (1) is determined in one dimension and for a fixed number of bosons on a finite lattice L with open boundaries. The numerical program we use is based on the DMRG algorithm; we refer the readers to Ref. [18] and to Appendix B for details on its implementation. In what follows we introduce and describe the observables we use in order to identify the quantum phases.

We identify superfluidity by a nonvanishing value of the single-particle correlations. In turn, a phase is incompressible (insulator) when the single-particle correlations vanish and there is a finite energy gap between the ground and the excited states in the thermodynamic limit. In order to gain information on the properties of the superfluid phase, we analyze the Fourier transform of the single-particle correlations, the so-called single-particle structure form factor, that is defined as [26]

$$M_1(k) = \frac{1}{L^2}\sum_{i,j} e^{ik(i-j)}\langle \hat{a}_i^\dagger \hat{a}_j\rangle, \tag{7}$$

where $\langle\cdot\rangle$ denotes the expectation value over the ground state. This quantity can be experimentally revealed by means of time-of-flight measurements [3]. Depending on the value of k at which $|M_1(k)|$ reveals a maximum, off-diagonal order can exhibit modulations in the phase. In the absence of the cavity, the ground-state superfluid is spatially homogeneous and characterized by a nonvanishing value of $M_1(k)$ at $k = 0$.

The superfluid (SF) phase acquires further features in the presence of the cavity field, depending on whether the expectation values $\langle\hat{D}\rangle$ and/or $\langle\hat{B}\rangle$ [compare Eqs. (4) and (5)] are different from zero in the thermodynamic limit. For this purpose we identify the order parameters

$$\mathcal{O}_D = \frac{1}{L}|\langle\hat{D}\rangle|, \tag{8}$$

$$\mathcal{O}_B = \frac{1}{2L}|\langle\hat{B}\rangle|\,, \tag{9}$$

which can be measured by detecting the light at the cavity output [8,36–38]. The order parameter $\mathcal{O}_D$ signals the onset of density modulation (even-odd population imbalance), while $\mathcal{O}_B$ signals the formation of dimers along the lattice [17], namely, a so-called dimerized or bond-ordered state [39,40]. In addition to the "normal" SF, the emerging SF phases can be lattice supersolid (SS) in the presence of diagonal long-range order ($\mathcal{O}_D \neq 0$ and $\mathcal{O}_B = 0$); bond SF (BSF) for homogeneous density and bond order ($\mathcal{O}_D = 0$ and $\mathcal{O}_B \neq 0$), or bond supersolid (BSS) when both order parameters are nonvanishing. The phases and the corresponding order parameters are summarized in Table I. The onsets of these gapless phases, i.e., SS, BSF, and the BSS, occur due to a spontaneous breaking of a discrete $\mathbb{Z}_2$ lattice translational symmetry. Such a spontaneous discrete symmetry breaking is captured by the twofold ground-state degeneracy in these phases (Sec. III E).

TABLE I. Table of the quantum phases of the ground state of Eq. (1), of their acronyms, and of the corresponding behavior of the order parameters.

Phase	Abbreviation	$\mathcal{O}_D$	$\mathcal{O}_B$	$\max\|M_1(k)\|$
Mott-insulator	MI	0	0	0
Density wave	CDW	$\neq 0$	0	0
Bond insulator	BI	0	$\neq 0$	0
Superfluid	SF	0	0	$M_1(0)$
Supersolid	SS	$\neq 0$	0	$M_1(0)$
Bond superfluid	BSF	0	$\neq 0$	$M_1(\pm\frac{\pi}{2})$
Bond supersolid	BSS	$\neq 0$	$\neq 0$	$M_1(\pm\frac{\pi}{2})$

The insulating phases, having vanishing $M_1(k)$ in the thermodynamic limit, are classified according to the values of the population imbalance and of the bond order parameters. The bond insulator (BI) is characterized by $\mathcal{O}_B \neq 0$, the charge-density wave (CDW) by $\mathcal{O}_D \neq 0$, while in the Mott insulator (MI) all order parameters here discussed vanish (see Table I). Similarly to the SS, BSF, or BSS phases, the insulating BI and CDW phases are also $\mathbb{Z}_2$-symmetry-broken phases. We remark that we have also determined the parity and string order parameters [41,42] in the resulting phases: for the parameter regimes considered we do not find signatures of the Haldane insulator (cf. Ref. [18]). This is consistent with other numerical studies on globally interacting systems [43].

III. GROUND-STATE PHASE DIAGRAM

We determine the phase diagrams for fixed densities as a function of the ratios U_1/U and t/U that we vary as previously specified. We consider in particular the densities $\rho = 1/2$ and $\rho = 1$ since they are commensurate with the long-range potential; thus they can give rise to insulating phases in addition to the gapless ones. In our model the ratio U_1/U controls the onset of structures that support the buildup of an intracavity field, while t/U determines the strength of quantum fluctuations. We sweep the ratio U_1/U from positive to negative values for different ϕ. Depending on ϕ we rescale U_1 by the maximum between the coefficients z^2 and y^2 [i.e., $\max(z^2, y^2)$], thus giving the effective strength of the cavity-induced interaction. The ground-state phase diagram is calculated by means of the DMRG algorithm with open boundary conditions.

In the following we present the phase diagram for a finite system of size $L = 60$ sites and identify the transition lines when the corresponding order parameter exceeds a threshold value: The line separating the incompressible and the compressible phases is set at the threshold value $\max|M_1(k)| = 0.1$. Bond and density-wave order are signaled by $\mathcal{O}_D > 0.02$ and $\mathcal{O}_B > 0.02$, respectively. We also analyze the order parameters across different transitions for different system sizes

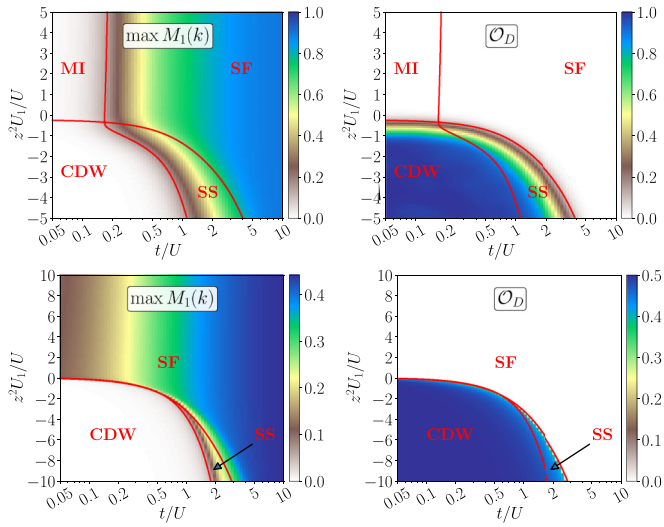

FIG. 2. Color plots of the phase diagrams in the plane U_1/U and t/U for $\phi = 0$ and density $\rho = 1$ (upper row) and $\rho = 1/2$ (lower row). The subplots show the maximum of $|M_1(k)|$ (left panels) and the density-wave order parameter (right panels); the phases are identified according to Table I. In the CDW phase two neighboring sites forming a unit cell have occupations $n_i = 2\rho$, $n_{i+1} = 0$, where $\rho = 1/2, 1$. Note that the interaction strength U_1 in the plots is scaled by z^2. The phase diagrams are obtained using DMRG on a lattice with size $L = 60$ and open boundaries. Here, t/U is varied from 0.01 to 1 in a logarithmic scale in 101 steps, while U_1/U is varied from -20 to 20 in uniform steps of width 0.1.

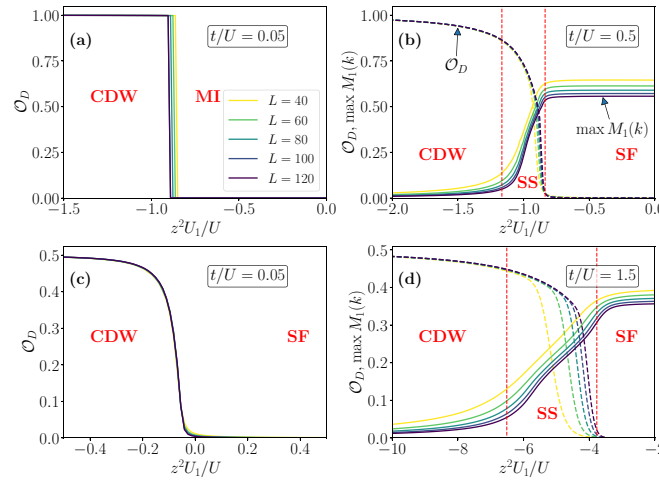

FIG. 3. The order parameters $\mathcal{O}_D$ and $|\max M_1(k)|$ as a function of U_1/U for $\phi = 0$, fixed t/U (as specified in the panels), and different system sizes $L \in [40, 120]$ [see legend in (a)]. The upper (lower) panels give the observables' behavior at density $\rho = 1$ ($\rho = 1/2$) across different phase transitions. The red vertical lines indicate the value of U_1/U at which we identify a phase transition; the corresponding phases are reported. For $\rho = 1$ (a) the MI-CDW transition is first-order discontinuous, while (b) the SF-SS transition is continuous and the CDW-SS transition is either continuous or a crossover. In the case of $\rho = 1/2$ (c) the SF-CDW and (d) the SF-SS transitions are continuous, while the SS-CDW transition could be either continuous or a crossover.

$L \in [40, 120]$ in order to determine the nature of the phase transitions and to verify the stability of the phase diagram with the varying system size. We finally determine the central charge of the bond-ordered gapless phases, BSF and BSS, that are due to the global interactions.

A. Phase diagrams for $\phi = 0$

For $\phi = 0$ the cavity-induced interactions in the extended Bose-Hubbard Hamiltonian consist solely of global density-density interactions. These interactions are periodic, with a periodicity that is twice the lattice periodicity. The corresponding phase diagram has been extensively studied in the literature for attractive interactions, corresponding to negative values of U_1 [8–12,17]. In this case the cavity potential favors the formation of ordered structures which support photon scattering into the cavity. For U_1 positive, on the other hand, the cavity-induced potential is repulsive and the energy is minimized for uniform densities, at which $\mathcal{O}_D$ vanishes.

Figure 2 displays the maximum of $|M_1(k)|$, signaling superfluidity, and the density-wave order parameter $\mathcal{O}_D$. For positive U_1 and for half filling the ground state remains in a SF phase for the whole t/U parameter range, while at unit density we find the MI-SF transition. Interestingly, the transition line slightly depends on the value of U_1 and in particular is shifted to larger values of t/U as U_1 increases: the repulsive cavity interaction tends to stabilize the incompressible phase.

The situation is different for attractive global interactions ($U_1 < 0$). Here, we identify the transition line $U_1^{(c)}$ separating the homogeneous phase from the density wave, which is a monotonously increasing function of t/U. The transition line qualitatively agrees with the one found by means of a mean-field ansatz for a grand-canonical ensemble [12]: At half-filling it vanishes at $t/U = 0$, $U_1^{(c)}(0) = 0$, while at unit density $U_1^{(c)}(0) < 0$. A direct transition between SF and the incompressible CDW is found at half filling and for $0 > U_1^{(c)} \gtrsim -U$, while for $U_1^{(c)} \lesssim -U$ a SS phase separates SF from CDW. At unit density there is no direct CDW-SF transition: The two phases are always separated either by a MI or by a SS phase. We also note that the area covered by the SS phase in parameter space is larger at unit density than at half filling.

By inspecting the behavior of the order parameters across different phase transitions (see Fig. 3), we deduce the nature of the transitions. Interestingly, for $\rho = 1/2$, the transitions SF-SS and SF-CDW are now characterized by a smooth change in the density-wave order parameter (lower panels of Fig. 3), signaling that these transitions are continuous. The CDW-SS transition, instead, is either continuous or a crossover. In the case of $\rho = 1$ (upper panels in Fig. 3), a jump in the order parameter $\mathcal{O}_D$ signals a discontinuous transition between the MI and the CDW phase.

B. Phase diagrams for $\phi = \pi/2$

We now discuss the case in which the cavity-mediated interactions are described by a global correlated hopping term. This configuration can be realized experimentally when the atoms are tightly confined at the nodes of the cavity field. In our model, this case corresponds to the choice $\phi = \pi/2$ in the cavity standing wave, resulting in $z = 0$ in Eq. (3).

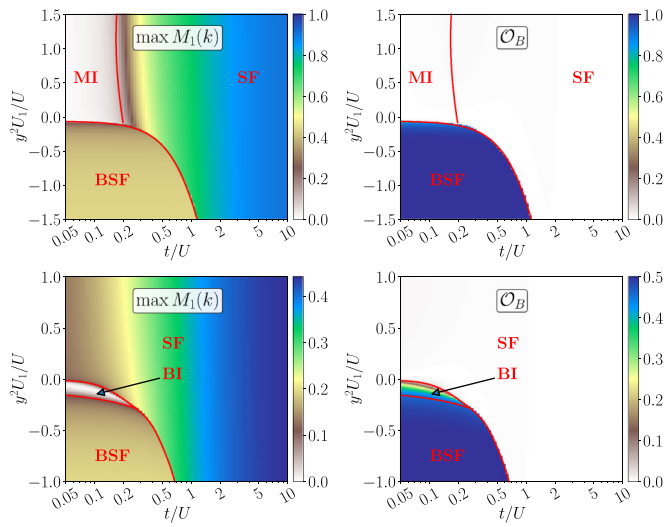

FIG. 4. Same as Fig. 2 but for $\phi = \pi/2$. Here, the right column displays the bond order parameter, $\mathcal{O}_B$. Note that the interaction strength U_1 in the plots is now rescaled by y^2 and we vary U_1/U in the range $[-400, 400]$ in steps of size 4 to generate the data.

Figure 4 displays the phase diagrams for density $\rho = 1$ (upper row) and $\rho = 1/2$ (lower row). For $U_1 > 0$ the ground state at half filling is SF. At unit density, the MI-SF transition line is visibly shifted to smaller values of t/U as U_1 increases: the size of the incompressible phase is reduced because the weight of quantum fluctuations at small t/U is enhanced due to the contribution of the global hopping. This trend is also visible in the color plot of the maximum of $M_1(k)$ for $\rho = 1/2$.

For $U_1 < 0$ we observe a transition from SF to bond order. Similar to the case $\phi = 0$, also here the transition shifts to larger values of t/U as $|U_1|$ increases: the cavity-induced correlated hopping tends to stabilize bond order, as expected. Remarkably, at $U_1 < 0$ we do not find incompressible phases for $\rho = 1$: in the considered parameter region the bond-ordered phase is BSF. Figure 5 displays the behavior of the order parameters at the transition between the BSF and the MI phase: both $M_1(k)$ and $\mathcal{O}_\mathcal{B}$ display a continuous behavior signaling a continuous transition. On the other hand, at higher t/U, the transition between the SF and the BSF phase is of first-order kind as visible in the discontinuity of $\max M_1(k)$ and $\mathcal{O}_\mathcal{B}$.

The phase diagrams at $\rho = 1/2$ differ from the ones at $\rho = 1$ due to the appearance of an insulating phase with bond order separating the BSF from the homogeneous phase. This phase is found for sufficiently small values of t/U. In Ref. [18] we showed that this is a topological insulator, which shares several analogies with the Su-Schrieffer-Heeger model. Inspection into the behavior of the order parameters shows that the transitions SF-BI and BI-BSF are continuous (Fig. 5), while the direct transition SF-BSF is discontinuous (cf. Ref. [18]).

C. Phase diagrams for $\phi = \pi/4$

We now discuss the ground-state phase diagrams emerging from the interplay of the density-density attractive potential

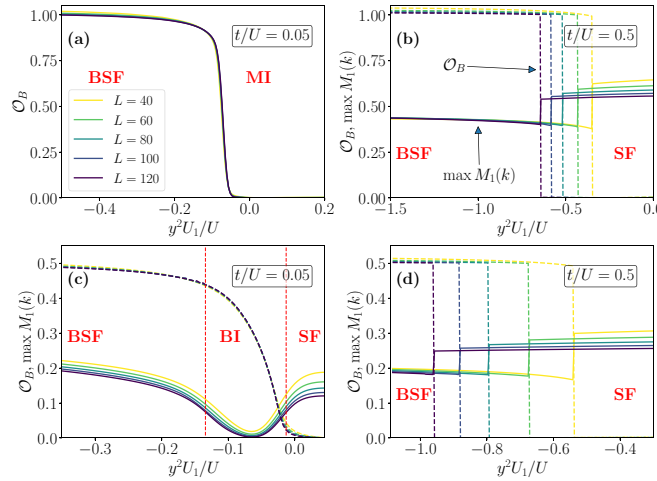

FIG. 5. The order parameters $\mathcal{O}_D$ and $|\max M_1(k)|$ as a function of U_1/U for $\phi = \pi/2$, fixed t/U (as specified in the panels), and different system sizes $L \in [40, 120]$ [see legend in (a)]. The upper (lower) panels give the observables' behavior at density $\rho = 1$ ($\rho = 1/2$) across different phase transitions. The red vertical lines indicate the value of U_1/U at which we identify a phase transition; the corresponding phases are reported. For $\rho = 1$ (a) the MI-BSF transition is continuous. Similarly, (c) for $\rho = 1/2$, the transitions SF-BI and BI-BSF are continuous. The SF-BSF transitions, on the other hand, are discontinuous for both (b) $\rho = 1$ and (d) $\rho = 1/2$.

and the correlated tunneling. We choose $\phi = \pi/4$ for which both z and y in Eq. (3) are different from zero, and recall that $z \sim 10|y|$ (see Fig. 1). Therefore, the coefficient scaling the correlated tunneling is one order of magnitude smaller than the coefficient scaling the cavity-induced potential term.

Figure 6 displays the order parameters for SF, density-wave, and bond order for unit density and for half filling. For $U_1 > 0$ the behavior we observe is essentially the same as for $\phi = 0$. Instead, for $U_1 < 0$ the phase diagram becomes richer. In the first place, at small values of t/U we observe a transition from the homogeneous phases to an insulating phase with both density-wave and bond order. This transition occurs for both density $\rho = 1$ and $1/2$. The new phase is an insulator of dimers with population imbalance within the dimer. We dub this phase CDW+BI since both order parameters $\mathcal{O}_D$ and $\mathcal{O}_B$ are nonzero. As visible in Fig. 7, the transition from the SF or SS to the CDW+BI at unit density is continuous, while the MI to the CDW+BI transition is discontinuous. For $\rho = 1/2$, instead, all the transitions are continuous or crossovers. At larger tunneling rates t/U the CDW+BI phase undergoes a transition to a SS phase for both $\rho = 1$ and $1/2$. The SS phase is signaled by the nonzero values of the maximum of $M_1(k)$ and by the vanishing value of the bond order parameter $\mathcal{O}_B$. The density-wave order parameter, instead, stays finite across the transition. We note that the transition CDW+BI to SS is continuous (or a crossover) for both unit density and half filling (Fig. 7). The SS phase is then separated from the SF phase by a continuous transition for both $\rho = 1$ and $1/2$ (analogously to the $\phi = 0$ geometry).

We now discuss the phases encountered keeping t/U fixed and tuning U_1/U to larger values along the negative axis. At unit density we observe a transition from CDW+BI to a compressible phase that has both density-wave and bond

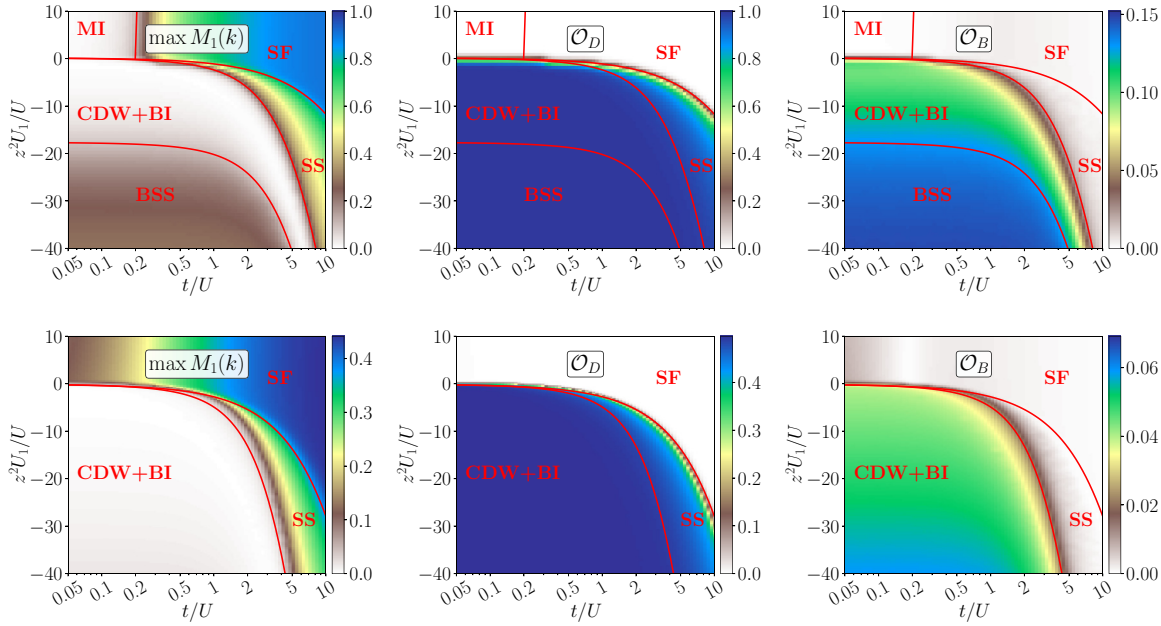

FIG. 6. Color plots of the phase diagrams in the plane U_1/U and t/U at $\phi = \pi/4$ and for density $\rho = 1$ (top) and $\rho = 1/2$ (bottom). The subplots show the maximum of $|M_1(k)|$ (left panels), the density-wave order parameter (central panels), and the bond order parameter (right panels); the phases are labeled according to Table I. The phase diagrams are calculated using DMRG on a lattice with $L = 60$ sites and open boundary conditions, where we have varied U_1/U from -200 to 200 in steps of size 2. Note that the interaction strength U_1 is scaled by z^2 in all subplots.

order. This phase is a SS phase exhibiting dimers—the BSS phase. Hence, at unit density and for low tunneling rates, large cavity-mediated interactions promote superfluidity, which at first sight seems counterintuitive. Interestingly, for the parameter window we have considered, we do not find a BSS phase at half filling. However, from the pattern of $M_1(k)$, we suspect that the BSS will also appear at half filling but at larger negative values of U_1/U.

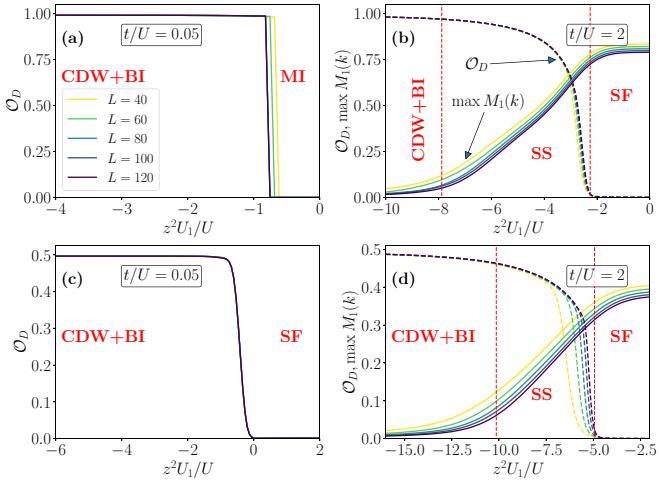

FIG. 7. The order parameters, $\mathcal{O}_D$ and $|\max M_1(k)|$, as a function of U_1/U for $\phi = \pi/4$, fixed t/U (as specified in the panels), and different system sizes $L \in [40, 120]$ [see legend in (a)]. The upper (lower) panels give the observables' behavior at density $\rho = 1$ ($\rho = 1/2$) across different phase transitions. The red vertical lines indicate the value of U_1/U at which we identify a phase transition; the corresponding phases are reported. For $\rho = 1$ (a) the MI to CDW+BI transition is first-order discontinuous, while (b) the SF-SS transition is continuous. The CDW+BI to the BSS transition in (a) is either continuous or a crossover. In the case of $\rho = 1/2$, the (c) SF to CDW+BI and (d) SF-SS transitions are continuous, while (d) the SS to CDW+BI transition is either continuous or a crossover.

D. Discussion

The phase diagrams for the three geometries have been also analyzed in Ref. [17] using exact diagonalization and small chains. In this work, we refrained from making a systematic comparison of our predictions with the results of Ref. [17]. In fact, our results are qualitatively and quantitatively different in most regions of the phase diagram. We believe that the discrepancy is mainly due to the very small size considered in Ref. [17]. To give a few examples, in Ref. [17] and at half filling the authors reported insulating phases for $U_1 > 0$, while instead the phase we find is always SF. Other phases, such as the superfluid dimer (SFD) dimers (that would here correspond to a sort of BSF phase) are reported in regions of the phase diagram where the DMRG predicts different ground-state phases. A Gutzwiller mean-field analysis confirms the DMRG result and often finds that the SFD (or BSF) phase in those regions is a metastable, excited state.

Remarkably, the phase diagram in Fig. 3 at $\rho = 1/2$ is in qualitative agreement with the mean-field predictions for a grand-canonical ensemble [9,12], despite the fact that in the present paper it has been determined using DMRG in one dimension. There are instead qualitative differences when comparing the phase diagram at unit density. For $\phi = \pi/2$ an analysis based on a Gutzwiller mean field for a canonical ensemble qualitatively reproduces the DMRG phase diagram for $\rho = 1$. It does not capture, however, the BI phase at half filling (see Ref. [18]).

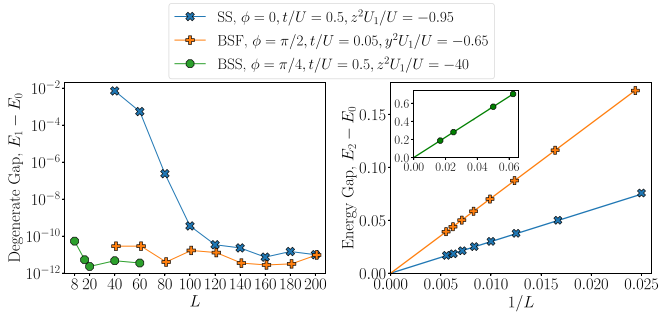

FIG. 8. The energy gaps in the SS, the BSF, and the BSS phase at unit filling. In the left panel, we plot the energy gap between the ground and the first excited states ($E_1 - E_0$) as a function of the system size L confirming the ground-state degeneracy in these phases. The right panel shows the gap between the ground and the second excited states ($E_2 - E_0$) that decays to zero in the thermodynamic limit as $\sim 1/L$, confirming the gapless character of the phases. Here we consider an even number of sites for the SS phase and an odd number of sites for the BSF phase with open boundary conditions, while for the BSS phase we impose periodic boundary conditions with even number of sites.

E. Symmetry-broken gapless phases

We have shown that the attractive cavity potential stabilizes inhomogeneous gapless phases, the SS, the BSF, and the BSS phase. These phases have long-range diagonal order, signaled by the nonvanishing order parameters $\mathcal{O}_D$ and/or $\mathcal{O}_B$, and off-diagonal correlations that decay algebraically with the distance. The long-range order in these three gapless phases manifests itself due to a spontaneous breaking of discrete $\mathbb{Z}_2$ lattice translational symmetry by doubling of the unit cell. A way to verify such a spontaneous symmetry breaking is by checking the ground-state degeneracy for finite system sizes. For spontaneous $\mathbb{Z}_2$ symmetry breaking, the energy gap between the ground state and the first excited state must fall to zero much faster than $\sim 1/L$ (ideally, the gap should diminish exponentially in the system size), while the spectral gap, as measured by the gap between the ground state and the second excited state should vanish as $\sim 1/L$ in a gapless phase.

In the SS phase ($O_D \neq 0$), the order develops in the sites by $\mathbb{Z}_2$ symmetry breaking, and therefore the ground state must be twofold degenerate for an even number of sites for large enough system sizes. In the left panel of Fig. 8 we plot the degenerate gap, i.e., the gap between the ground and the first excited states ($E_1 - E_0$). The gap reaches the numerical precision ($\lesssim 10^{-10}$) set by DMRG simulations as we increase the system size. The right panel shows the gap between the ground and the second excited states ($E_2 - E_0$) as a function of $1/L$. It decays to zero as $\sim 1/L$, confirming the gapless nature of the phase. The number of sites will be odd when analyzing the BSF phase ($O_B \neq 0$), because the order develops in the bonds. Therefore, an even number of bonds (and hence odd number of sites) is needed to observe the ground-state degeneracy. In Fig. 8 we verify the ground-state degeneracy along with gapless nature of the BSF phase for an odd number of sites ($L = 41, 61, 81, \ldots$). In the BSS phase (O_D and O_B both are nonzero), the order develops in both sites and bonds. Therefore, we need to impose periodic boundary conditions with an even number of sites and/or bonds to observe the degeneracy. We find that, even for system size $L = 8$ with periodic boundary conditions, the gap in the BSS phase reaches numerical precision (Fig. 8); thus we expect that it vanishes in the thermodynamic limit.

F. Scaling of the entanglement entropy in the gapless bond-ordered phases

Let us now analyze the two bond superfluid phases we find, namely, the BSF for $\phi = \pi/2$ and the BSS for $\phi = \pi/4$ and at unit density. We determine in particular the scaling of the entanglement entropy with the system size. The entanglement entropy of a lattice partition comprising the sites $\ell = 1, \ldots, j$ is defined as

$$\mathcal{S}_j = -\mathrm{Tr}[\rho_j \ln \rho_j], \tag{10}$$

where j denotes the bond that separates the system into two parts, and $\rho_j = \mathrm{Tr}_{j+1,j+2,\ldots,L} |\psi\rangle \langle\psi|$ is the reduced density matrix obtained from the ground state $|\psi\rangle$ by tracing out the degrees of freedom of the second partition. In a gapless critical system with open boundary conditions the entanglement entropy scales with the size of the block of consecutive sites according to [44–46]

$$\mathcal{S}_j = \frac{c}{6} \ln \left[\frac{2L}{\pi} \sin(\pi j/L) \right] + b', \tag{11}$$

where c is the central charge of the corresponding conformal field theory (CFT) that describes the criticality and b' is a nonuniversal constant. In Bose-Hubbard models with short-range interaction, the gapless critical phases, e.g., SF and SS phases, obey the entropy scaling formula (11) with $c = 1$ that corresponds to the CFT of free compactified bosons described by Tomonaga-Luttinger liquid theory [47]. However, the fate of such an entropy scaling in the presence of infinite-range global interactions is still an open question. This question is particularly intriguing when considering the BSF and BSS phases in our study, since these gapless phases are due to the infinite-range interactions.

Figure 9 displays the entanglement entropy as a function of the chord length $\ln[\frac{2L}{\pi} \sin(\pi j/L)]$ in the BSF and the BSS phases for system sizes $L = 60$, 80, 100, and 120. Interestingly, although these phases appear when the global correlated tunneling and the potential dominate over the short-ranged counterparts, the entropy still shows a linear growth with respect to the chord length and hence a logarithmic divergence with respect to the system size. Moreover, the corresponding central charges are $c \simeq 1$, as in the cases of SF and SS phases of the Bose-Hubbard model with short-range interactions.

IV. CONCLUSIONS

In this work we have presented a numerical analysis of the quantum phases of bosons in an extended Bose-Hubbard model with global density-density interactions and global correlated tunneling. The quantum phases have been studied for a one-dimensional lattice and for configurations which are consistent with the setups of cavity quantum electrodynamics, where the global interactions are mediated by multiple scattered photons in the dispersive optomechanical regime [8,48]. The geometry we considered permits one to tune the relative strength of the coefficients scaling the long-range

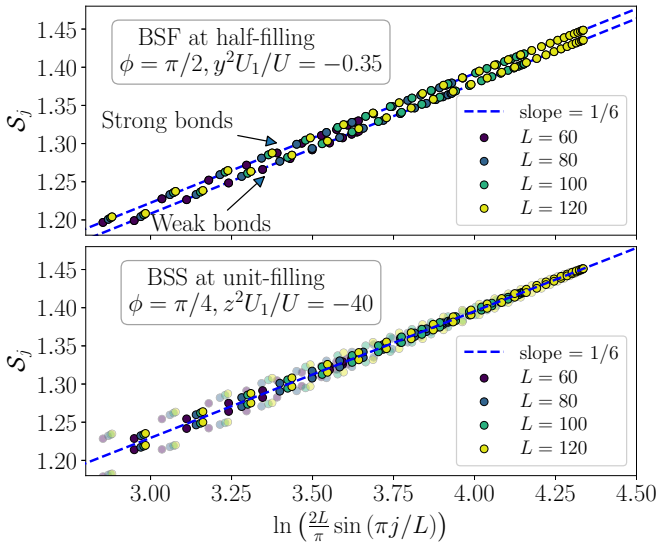

FIG. 9. The scaling of entanglement entropy in the BSF (top panel) and the BSS (bottom panel) phases according to the formula in Eq. (11). For both cases $t = 0.5U$; the other parameters are given in the legends. The numerical fits yield $c = 1.00(2)$ and $c = 0.99(5)$, respectively. Note that for the BSF we get two distinct straight lines, both having a slope of $\sim 1/6$, corresponding to the entanglement entropy when the partition is cut at a strong and at a weak bond, respectively. In the BSS the fluctuations of the entropy with respect to the mean slope of $1/6$ are due to the modulations of densities and bonds across the system.

potential and the correlated tunneling terms in the extended Bose-Hubbard model

In the geometry where correlated tunneling vanishes, the cavity-mediated potential induces density-wave order and the phase diagrams we obtain are consistent with the ones predicted in higher dimensions [9–12]. In the geometries where correlated tunneling cannot be discarded, we find phases with bond order. These phases are analogous to valence bond solids and fluids in spin systems [39]. We remark that bond-ordered phases are also present in other systems, for instance in zigzag optical lattices with density-dependent gauge fields [49], in spin-1/2 dipolar Fermi gases in lattice potentials [50], and in honeycomb lattices with anisotropic tunneling [40]. In contrast to those models, here the bond order is a self-organized phase induced by photon-atom interactions in a cavity.

The interplay of the cavity-induced potential and correlated tunneling gives rise to phases that can simultaneously exhibit density-wave and bond order. Remarkably, at low tunneling and unit density the cavity interactions favor a bond supersolid, where one would otherwise expect an incompressible phase. We have analyzed the nature of these self-organized bond superfluid phases for exemplary parameter regimes by means of the scaling of the entanglement entropy and found that these phases have the same central charge as the superfluid phases of short-ranged Bose-Hubbard models.

Bond and density-wave order correspond to self-organized patterns which scatter coherently into the cavity mode. Correspondingly, they are associated with the onset of an intracavity field that is proportional to density-wave and bond-order parameters and can be measured at the cavity output [13,35,38]. Superfluidity can be revealed by time-of-flight measurements [35]. The low energy gap could be determined by means of a pump-probe experiment.

Bond order in these dynamics can be often understood in terms of interference between single-particle hopping and correlated tunneling [18,26]. The very same interference is at the basis of the phases observed in one dimension for correlated tunneling with short-range interactions, even though the resulting phases are different [25,26]. In two dimensions the phases result from an interesting interplay between frustration and quantum interference [27,51]. The extension of these dynamics to global interactions is nontrivial and will be subject of future works.

ACKNOWLEDGMENTS

R.K. and G.M. acknowledge the support of the Deutsche Forschungsgemeinschaft (DFG, German Research Foundation), Project-ID 429529648 TRR 306 QuCoLiMa ("Quantum Cooperativity of Light and Matter") and Priority Program SPP1929 GiRyd ("Giant Interactions in Rydberd Systems"). They also acknowledge the support of the German Ministry of Education and Research (BMBF) via the QuantERA projects "QTFLAG" and "NAQUAS." Project NAQUAS has received funding from the QuantERA ERA-NET Cofund in Quantum Technologies implemented within the European Union's Horizon 2020 Programme. T.C. and J.Z. acknowledge the support of PL-Grid Infrastructure and the National Science Centre (Poland) under project Opus 2019/35/B/ST2/00034 (J.Z.) and Unisono 2017/25/Z/ST2/03029 (T.C.) realized within the QuantERA ERA-NET QTFLAG collaboration. The DMRG simulations have been performed using the ITensor library [52].

APPENDIX A: ON THE EXTENDED BOSE-HUBBARD MODEL OF CAVITY QUANTUM ELECTRODYNAMICS

The extended Bose-Hubbard model of Eq. (1) is found by performing the Wannier expansion of the Hamiltonian $\hat{H}_{\rm eff} = \hat{H} + \hat{H}_{\rm C}$ as a function of the bosonic field operators $\Psi(\mathbf{r})$ with $[\Psi(\mathbf{r}), \Psi^\dagger(\mathbf{r}')] = \delta(\mathbf{r} - \mathbf{r}')$. The Hamiltonian term $\hat{H}$ consists of the kinetic energy, the potential of the optical lattice, and contact interaction between the atoms:

$$\hat{H} = \int d^3\mathbf{r}\hat{\Psi}^\dagger(\mathbf{r})\left(-\frac{\hbar^2}{2m}\nabla^2 + V_{\rm trap}\right)\hat{\Psi}(\mathbf{r}) \tag{A1}$$

$$+\frac{g}{2}\int d^3\mathbf{r}\hat{\Psi}^\dagger(\mathbf{r})^2\hat{\Psi}(\mathbf{r})^2\,, \tag{A2}$$

while the effect of the atom-cavity coupling is described by the effective long-range Hamiltonian [13,34]

$$\hat{H}_C = \frac{U_1}{L}\left(\int d^3\mathbf{r}\hat{\Psi}^\dagger(\mathbf{r})h(\mathbf{r})\hat{\Psi}(\mathbf{r})\right)^2, \tag{A3}$$

where $h(\mathbf{r})$ is the spatial mode function of the cavity field, with $\max|h(\mathbf{r})| = 1$. Hamiltonian (A3) is obtained by eliminating the cavity field assuming that this evolves on a faster time scale than the atomic motion. The details of the derivation of Eq. (A3) starting from the full atom-photon master equation (that accounts for cavity losses) have been reported and

discussed in Refs. [13,33,36,38] (see also Ref. [53] for a systematic semiclassical treatment). We note that in Eq. (A3) we have neglected a term resulting from the dynamical Stark shift of the cavity field. We further remark that the coefficient U_1 is proportional to the intensity of a transverse laser field, driving the atoms, and that its sign is experimentally controlled by the sign of the detuning between the cavity and laser frequency [13,33,54].

In our work we assume a trapping potential of the form $V_{\text{trap}} = V_{\text{lat}}(x) + \frac{m\omega^2}{2}(y^2 + z^2)$ with ω the trap frequency and

$$V_{\text{lat}}(x) = V_0 \sin^2(kx).$$

The trap frequency ω is chosen so that the atoms can be assumed to be in the ground state of the transverse trapping potential. In the single-band approximation the Wannier expansion of the bosonic field reads

$$\Psi(\mathbf{r}) = \sum_j w_j(x)\psi_0(y,z)\hat{a}_j, \tag{A4}$$

where $w_j(x)$ are one-dimensional Wannier functions centered on j sites along the x direction, $\psi_0(y,z)$ is the ground-state wave function of the transverse harmonic trap, and $\hat{a}_j$ annihilates a boson at site j and in the ground state of the harmonic trap.

The cavity spatial mode function is here assumed to be given by its expression in the paraxial approximation,

$$h(\mathbf{r}) = \cos(kx + \phi),$$

assuming that the transverse size of the atomic gas is much smaller than the mode waist.

By using Eq. (A4) in Hamiltonian $\hat{H}$ and performing the integrals as outline in Refs. [13,34,36], one obtains the Bose-Hubbard Hamiltonian of Eq. (1).

APPENDIX B: DETAILS ABOUT DMRG SIMULATIONS

The DMRG algorithm [28,29] that we employ is based on a matrix product state (MPS) ansatz [30,31] to find the ground state and low-lying excited states of the system. We employ the global $U(1)$ symmetry corresponding to the conservation of the total number of particles [55,56]. For that purpose, we use the ITensor C++ library [52] where the matrix product operator (MPO) for the all connected long-range Hamiltonian can be constructed exactly [57,58] using the AutoMPO class. In our Hamiltonian (1) [with Eq. (3)], when both $\hat{B}$ and $\hat{D}$ terms are nonzero the MPO bond dimension turns out to be 13. The maximum number of bosons (n_0) per site has been truncated to 6.

We consider random entangled states, $|\psi_{\text{ini}}\rangle = \frac{1}{\sqrt{50}}\sum_{i=0}^{49}|\psi_i^{\text{rand}}\rangle$, where $|\psi_i^{\text{rand}}\rangle$ are random product states with fixed density (either $\rho = 1$ or $1/2$), as our initial states for the DMRG algorithm. The maximum bond dimension of MPS has been restricted to $\chi_{\max} = 600$, so that the discarded weights of the singular values remain below 10^{-10} even in the gapless phases for system sizes up to $L \leqslant 120$. It is to be noted that in the case of small system sizes or the gapped phases, the final bond dimension may not reach $\chi = 600$, as in our DMRG sweeps we discard any singular values having weights below 10^{-12}. We verify the convergence of the DMRG algorithm by checking the deviations in energy in successive DMRG sweeps. When the energy deviation in successive sweeps falls below 10^{-12}, we conclude that the resulting MPS is the ground state of the system.

To obtain low-lying excited states, as in Fig. 8, we first shift the Hamiltonian by a weight factor multiplied with the projector of the previously found state. To be precise, for finding the nth excited state $|\psi_n\rangle$, we search for the ground state of the shifted Hamiltonian,

$$\hat{H}' = \hat{H} + W\sum_{m=0}^{n-1}|\psi_m\rangle\langle\psi_m|, \tag{B1}$$

where W should be guessed to be sufficiently larger than $E_n - E_0$.

[1] M. P. A. Fisher, P. B. Weichman, G. Grinstein, and D. S. Fisher, Phys. Rev. B **40**, 546 (1989).
[2] D. Jaksch, C. Bruder, J. I. Cirac, C. W. Gardiner, and P. Zoller, Phys. Rev. Lett. **81**, 3108 (1998).
[3] M. Greiner, O. Mandel, T. Esslinger, T. W. Hänsch, and I. Bloch, Nature (London) **415**, 39 (2002).
[4] I. Bloch, J. Dalibard, and W. Zwerger, Rev. Mod. Phys. **80**, 885 (2008).
[5] M. Lewenstein, A. Sanpera, and V. Ahufinger, *Ultracold Atoms in Optical Lattices: Simulating Quantum Many-Body Systems* (Oxford University Press, Oxford, UK, 2012).
[6] S. Gopalakrishnan, B. L. Lev, and P. M. Goldbart, Phys. Rev. Lett. **107**, 277201 (2011).
[7] A. Periwal, E. S. Cooper, P. Kunkel, J. F. Wienand, E. J. Davis, and M. Schleier-Smith, Nature (London) **600**, 630 (2021).
[8] R. Landig, L. Hruby, N. Dogra, M. Landini, R. Mottl, T. Donner, and T. Esslinger, Nature (London) **532**, 476 (2016).
[9] N. Dogra, F. Brennecke, S. D. Huber, and T. Donner, Phys. Rev. A **94**, 023632 (2016).
[10] A. E. Niederle, G. Morigi, and H. Rieger, Phys. Rev. A **94**, 033607 (2016).
[11] T. Flottat, L. de Forges de Parny, F. Hébert, V. G. Rousseau, and G. G. Batrouni, Phys. Rev. B **95**, 144501 (2017).
[12] L. Himbert, C. Cormick, R. Kraus, S. Sharma, and G. Morigi, Phys. Rev. A **99**, 043633 (2019).
[13] S. Fernández-Vidal, G. De Chiara, J. Larson, and G. Morigi, Phys. Rev. A **81**, 043407 (2010).
[14] M. Maik, P. Hauke, O. Dutta, M. Lewenstein, and J. Zakrzewski, New J. Phys. **15**, 113041 (2013).
[15] O. Dutta, M. Gajda, P. Hauke, M. Lewenstein, D.-S. Luehmann, B. A. Malomed, T. Sowiński, and J. Zakrzewski, Rep. Prog. Phys. **78**, 066001 (2015).
[16] T. J. Elliott and I. B. Mekhov, Phys. Rev. A **94**, 013614 (2016).
[17] S. F. Caballero-Benitez and I. B. Mekhov, New J. Phys. **18**, 113010 (2016).

[18] T. Chanda, R. Kraus, G. Morigi, and J. Zakrzewski, Quantum **5**, 501 (2021).
[19] R. Strack and D. Vollhardt, Phys. Rev. Lett. **70**, 2637 (1993).
[20] J. E. Hirsch, Phys. B: Condens. Matter **199-200**, 366 (1994).
[21] J. C. Amadon and J. E. Hirsch, Phys. Rev. B **54**, 6364 (1996).
[22] K. P. Schmidt, J. Dorier, A. M. Läuchli, and F. Mila, Phys. Rev. Lett. **100**, 090401 (2008).
[23] K. P. Schmidt, J. Dorier, A. Läuchli, and F. Mila, Phys. Rev. B **74**, 174508 (2006).
[24] T. Sowiński, O. Dutta, P. Hauke, L. Tagliacozzo, and M. Lewenstein, Phys. Rev. Lett. **108**, 115301 (2012).
[25] K. Biedroń, M. Łącki, and J. Zakrzewski, Phys. Rev. B **97**, 245102 (2018).
[26] R. Kraus, K. Biedroń, J. Zakrzewski, and G. Morigi, Phys. Rev. B **101**, 174505 (2020).
[27] K. Suthar, R. Kraus, H. Sable, D. Angom, G. Morigi, and J. Zakrzewski, Phys. Rev. B **102**, 214503 (2020).
[28] S. R. White, Phys. Rev. Lett. **69**, 2863 (1992).
[29] S. R. White, Phys. Rev. B **48**, 10345 (1993).
[30] U. Schollwöck, Ann. Phys. **326**, 96 (2011).
[31] R. Orús, Ann. Phys. **349**, 117 (2014).
[32] T. Chanda, J. Zakrzewski, M. Lewenstein, and L. Tagliacozzo, Phys. Rev. Lett. **124**, 180602 (2020).
[33] H. Habibian, A. Winter, S. Paganelli, H. Rieger, and G. Morigi, Phys. Rev. Lett. **110**, 075304 (2013).
[34] H. Habibian, A. Winter, S. Paganelli, H. Rieger, and G. Morigi, Phys. Rev. A **88**, 043618 (2013).
[35] K. Baumann, C. Guerlin, F. Brennecke, and T. Esslinger, Nature (London) **464**, 1301 (2010).
[36] J. Larson, B. Damski, G. Morigi, and M. Lewenstein, Phys. Rev. Lett. **100**, 050401 (2008).
[37] K. Baumann, R. Mottl, F. Brennecke, and T. Esslinger, Phys. Rev. Lett. **107**, 140402 (2011).
[38] P. Sierant, K. Biedroń, G. Morigi, and J. Zakrzewski, SciPost Phys. **7**, 008 (2019).
[39] I. Affleck, T. Kennedy, E. H. Lieb, and H. Tasaki, Phys. Rev. Lett. **59**, 799 (1987).
[40] O. Jürgensen and D.-S. Lühmann, New J. Phys. **16**, 093023 (2014).
[41] E. G. Dalla Torre, E. Berg, and E. Altman, Phys. Rev. Lett. **97**, 260401 (2006).
[42] D. Rossini and R. Fazio, New J. Phys. **14**, 065012 (2012).
[43] J. Sicks and H. Rieger, Eur. Phys. J. B **93**, 104 (2020).
[44] C. Callan and F. Wilczek, Phys. Lett. B **333**, 55 (1994).
[45] G. Vidal, J. I. Latorre, E. Rico, and A. Kitaev, Phys. Rev. Lett. **90**, 227902 (2003).
[46] P. Calabrese and J. Cardy, J. Stat. Mech.: Theory Exp. (2004) P06002.
[47] M. A. Cazalilla, R. Citro, T. Giamarchi, E. Orignac, and M. Rigol, Rev. Mod. Phys. **83**, 1405 (2011).
[48] P. Zupancic, D. Dreon, X. Li, A. Baumgärtner, A. Morales, W. Zheng, N. R. Cooper, T. Esslinger, and T. Donner, Phys. Rev. Lett. **123**, 233601 (2019).
[49] T. Mishra, S. Greschner, and L. Santos, New J. Phys. **18**, 045016 (2016).
[50] M. Di Dio, L. Barbiero, A. Recati, and M. Dalmonte, Phys. Rev. A **90**, 063608 (2014).
[51] C. Zhang, J. Zhang, J. Yang, and B. Capogrosso-Sansone, Phys. Rev. A **103**, 043333 (2021).
[52] M. Fishman, S. R. White, and E. M. Stoudenmire, arXiv:2007.14822.
[53] J. Sebby-Strabley, M. Anderlini, P. S. Jessen, and J. V. Porto, Phys. Rev. A **73**, 033605 (2006).
[54] H. Ritsch, P. Domokos, F. Brennecke, and T. Esslinger, Rev. Mod. Phys. **85**, 553 (2013).
[55] S. Singh, R. N. C. Pfeifer, and G. Vidal, Phys. Rev. A **82**, 050301(R) (2010).
[56] S. Singh, R. N. C. Pfeifer, and G. Vidal, Phys. Rev. B **83**, 115125 (2011).
[57] G. M. Crosswhite, A. C. Doherty, and G. Vidal, Phys. Rev. B **78**, 035116 (2008).
[58] B. Pirvu, V. Murg, J. I. Cirac, and F. Verstraete, New J. Phys. **12**, 025012 (2010).